



Technical Note

Study on Daytime Atmospheric Mixing Layer Height Based on 2-Year Coherent Doppler Wind Lidar Observations at the Southern Edge of the Taklimakan Desert

Lian Su ¹ , Haiyun Xia ^{1,2,*}, Jinlong Yuan ², Yue Wang ², Amina Maituerdi ³ and Qing He ⁴

¹ School of Earth and Space Science, University of Science and Technology of China, Hefei 230026, China; kiwensu@mail.ustc.edu.cn

² School of Atmospheric Physics, Nanjing University of Information Science and Technology, Nanjing 210044, China

³ Xinjiang Uygur Autonomous Region Meteorological Service, Urumqi 830002, China

⁴ Institute of Desert Meteorology, China Meteorological Administration, Urumqi 830002, China

* Correspondence: hsia@ustc.edu.cn

Abstract: The long-term atmospheric mixing layer height (MLH) information plays an important role in air quality and weather forecasting. However, it is not sufficient to study the characteristics of MLH using long-term high spatial and temporal resolution data in the desert. In this paper, over the southern edge of the Taklimakan Desert, the diurnal, monthly, and seasonal variations in the daytime MLH (retrieved by coherent Doppler wind lidar) and surface meteorological elements (provided by the local meteorological station) in a two-year period (from July 2021 to July 2023) were statistically analyzed, and the relationship between the two kinds of data was summarized. It was found that the diurnal average MLH exhibits a unimodal distribution, and the decrease rate in the MLH in the afternoon is much higher than the increase rate before noon. From the seasonal and monthly perspective, the most frequent deep mixing layer (>4 km) was formed in June, and the MLH is the highest in spring and summer. Finally, in terms of their mutual relationship, it was observed that the east-pathway wind has a greater impact on the formation of the deep mixing layer than the west-pathway wind; the dust weather with visibility of 1–10 km contributes significantly to the formation of the mixing layer; the temperature and relative humidity also exhibit a clear trend of a concentrated distribution at about the height of 3 km. The statistical analysis of the MLH deepens the understanding of the characteristics of dust pollution in this area, which is of great significance for the treatment of local dust pollution.

Keywords: mixing layer height; lidar; Taklimakan Desert; dust weather; statistical analysis



Citation: Su, L.; Xia, H.; Yuan, J.; Wang, Y.; Maituerdi, A.; He, Q. Study on Daytime Atmospheric Mixing Layer Height Based on 2-Year Coherent Doppler Wind Lidar Observations at the Southern Edge of the Taklimakan Desert. *Remote Sens.* **2024**, *16*, 3005. <https://doi.org/10.3390/rs16163005>

Academic Editor: Yaoming Ma

Received: 1 July 2024

Revised: 3 August 2024

Accepted: 14 August 2024

Published: 16 August 2024



Copyright: © 2024 by the authors. Licensee MDPI, Basel, Switzerland. This article is an open access article distributed under the terms and conditions of the Creative Commons Attribution (CC BY) license (<https://creativecommons.org/licenses/by/4.0/>).

1. Introduction

The atmospheric mixing layer (ML) is a type of atmospheric boundary layer (ABL) where exchange processes between the atmosphere and surface occur through turbulent mixing [1]. Its height, known as the mixing layer height (MLH), can indicate the diffusion and dilution ability of atmospheric aerosol in the vertical direction and quantify the degree of turbulent mixing development [2]. The long-term continuous observation of the MLH is of great significance to the local air pollution forecasting and the formulation of air pollution policies.

The variation in MLH is significantly affected by the local weather system and meteorological conditions [3]. Dust weather is mainly distributed along the southern edge and hinterland of the Taklimakan Desert (TD) [4]. The study site of this paper is Min-Feng County, which is situated at the southern edge of the TD and the foot of the Kunlun Mountains. It is of great significance to study the ML at this site. On the one hand, the convergence of the east-west airflows at the study site leads to frequent wind-sand events [5,6],

and the health of local people is deeply impacted by dust weather [7]. According to statistics, the average annual dust days in MinFeng has reached 113.5 days [8], making it the place with the most frequent occurrence of dust weather in China. On the other hand, there is a widespread dust aerosol layer at a height of 3 km [9], the deep ML of higher than 3 km occurred frequently [10], and the number of days with an MLH exceeding 4 km is more than that of other meteorological stations in the TD during the summer [11]. It is significant that the dust aerosols here can rise into the free troposphere above 7 km, driven by the northern slope of the Tibetan Plateau (TP) [12,13], and can affect the climate of the TP and even the whole globe [14,15]. However, the MinFeng station was built in 2018 [16], and the previous studies on the ML in this region were relatively few, mostly focusing on summer and case studies [17,18]. There are few long-term high spatial and temporal resolution observations to reveal the variation characteristics of the local ML from monthly, seasonal, and annual perspectives.

At present, the MLH cannot be measured directly by instruments, and its estimation relies on the analysis of vertical profiles of the temperature, turbulence, or atmospheric composition [3]. The coherent Doppler wind lidar (CDWL) has the characteristics of high spatial and temporal resolution, a short blind area, and high detection height [19–22], which confirms the reliability of its estimation of MLH in various application scenarios [17,23–25].

In view of this, the CDWL was used to conduct a long-term stable observation experiment spanning up to 2 years in the MinFeng County, located in the TD, and the MLH was calculated. The relationship and variation between the MLH and the surface meteorological elements (SMEs) were statistically analyzed. This paper is organized as follows: the study site, data, and methods are described in Section 2. The variation in MLH and SMEs with time are analyzed in Section 3. The relationship between MLH and SMEs is analyzed in Section 4. Finally, a conclusion is drawn in Section 5.

2. Site, Data, and Methods

2.1. Site

The experiment was carried out at MingFeng (37.06° N, 82.69° E, elevation 1418 m), situated at the northern foot of Kunlun Mountain and the southern edge of TD, as shown in Figure 1. The mountains, gobi, desert, saline-alkali land, and alluvial fan plains are widely distributed in MinFeng county. Due to the blocking effect of the TP and the desert surrounded by three mountains, the water vapor sources in the territory of MinFeng are scarce. Furthermore, the east-west airflow converges here, resulting in frequent droughts, dry-hot winds, dust storms, and other disastrous weather in this region [26–28].

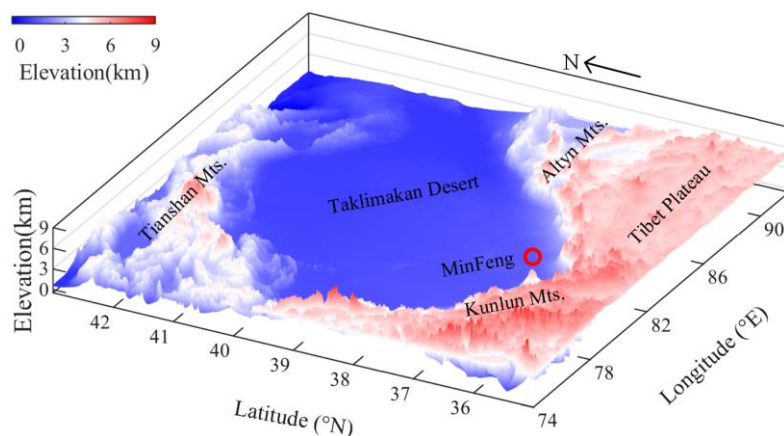


Figure 1. The 3D topographic map of Taklimakan Desert. The red circle represents the study site of MinFeng.

2.2. Data

Using the CDWL, a long-term stable observation experiment was conducted in the TD from July 2021 to May 2023. The wavelength and pulse energy of the CDWL are 1.5 μm and 130 μJ , respectively. During the experiment, the scanning elevation angle was fixed at 70° , the azimuth interval angle was set to 12° , and the velocity azimuth display (VAD) scanning mode with period of 1 min was continuously performed [29]. The key parameters of the CDWL are listed in Table 1. In the preprocessing stage, when the carrier-to-noise ratio (CNR) is below -18 dB, the lidar data involved in the MLH calculation are eliminated. The instrument calibration and potential data bias were described by Li and Wei [30,31]. According to the average sunrise and sunset time, the daytime period is defined as 08:00~21:00 Beijing time (BJT). The amount of MLH data included in the statistics reached 440 thousand groups.

Table 1. Key parameters of the CDWL.

Parameter	Value
Wavelength	1.5 μm
Pulse energy	130 μJ
Pulse duration	200 ns
Pulse repetition frequency	10 kHz
Diameter of telescope	100 mm
Radial spatial resolution	30 m
Azimuth scanning range	$0\text{--}360^\circ$
Elevation angle	70°
Sample rate of ADC	500 MS/s

The MinFeng weather station provides SMEs from July 2021 to July 2023, including near-surface ten-minute average wind speed (WS), near-surface ten-minute average wind direction (WD), atmospheric temperature (T), relative humidity (RH), and horizontal visibility (VIS). The temporal resolution of SMEs is 1 h, and the sample size is 9883 groups.

2.3. Methods

The high spatial and temporal resolution characteristics of CDWL data can be utilized to estimate the turbulent kinetic energy dissipation rate (TKEDR) at different heights [32–34]. To calculate the TKEDR while taking into account the temporal resolution, the CDWL used the VAD scanning mode with the azimuth interval of 12° . The TKEDR threshold method is one of the effective approaches to estimate the MLH [35,36]. The threshold of TKEDR in this paper is set at $10^{-4} \text{ m}^2 \text{ s}^{-3}$. When there is a cloud, the HWCT (Haar wavelet covariance transform) method is first used to identify the cloud [19]; secondly, when the cloud coverage time exceeds 10 min and causes a drastic change in the MLH, the MLH data during this period are removed. The error analysis for calculating TKEDR and MLH was conducted by Viktor A. Banakh [32,37]. The same type of CDWL instrument has been applied and verified for the estimation of TKEDR and MLH in various application scenarios [19,38,39].

The typical TKEDR and MLH inversion results are presented in Figure 2. At night, the radiation cooling of the desert underlying surface facilitates the formation of the inversion layer [40]. Compared to the night, the MLH during the daytime (8:00~21:00 BJT) can better reflect the dust pollution. In summer, the MLH exceeded 4 km (Figure 2(31–33)). In the winter (Figure 2(46–54)), the MLH is generally lower than 1 km. To investigate the variation characteristics of the ML, all the MLH data were statistically analyzed.

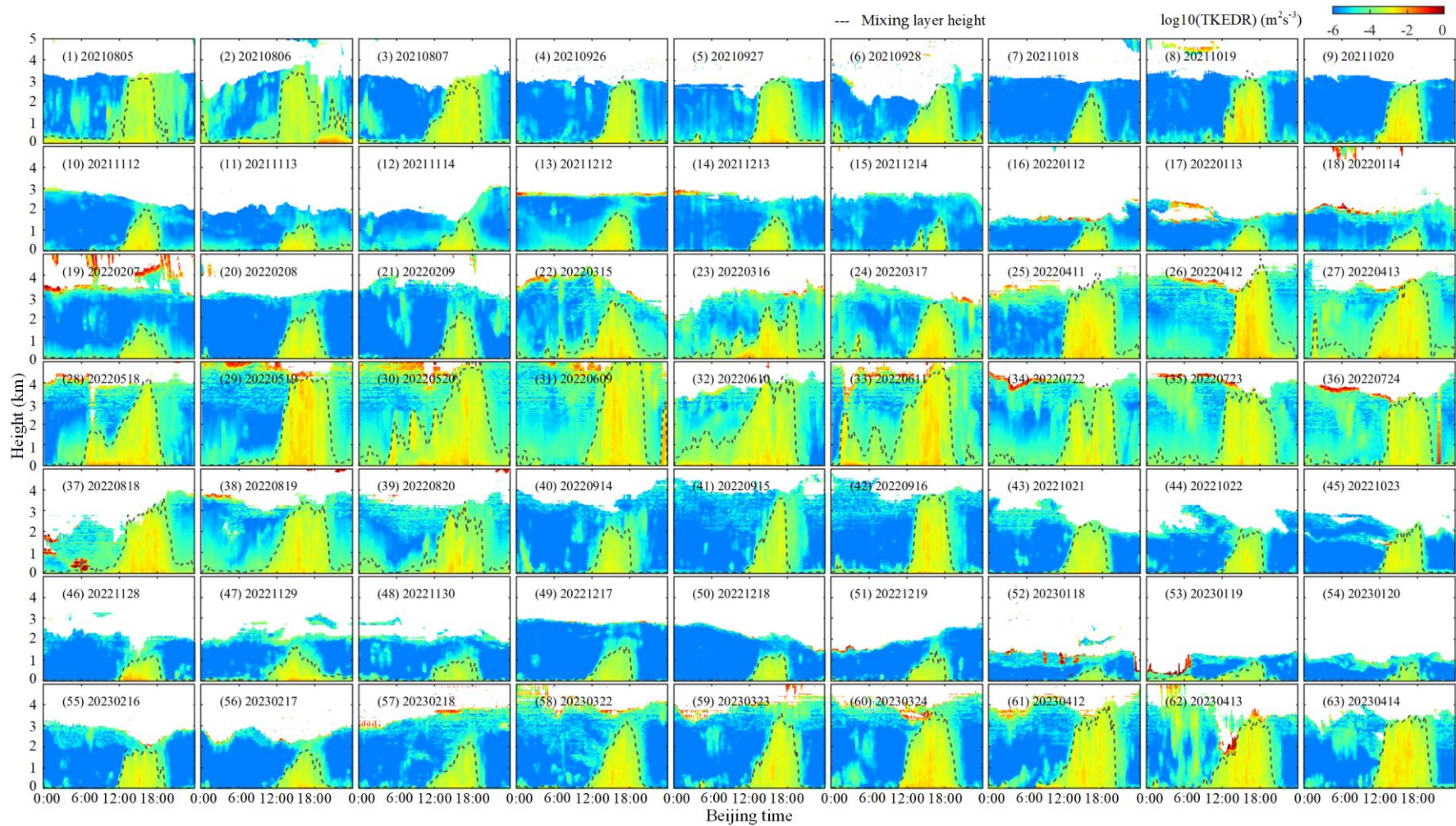


Figure 2. The typical atmospheric mixing layer height results calculated by using the TKEDR threshold method.

3. Monthly and Seasonal Variation Characteristics

3.1. Wind Speed and Wind Direction

In the hinterland of the TD, the threshold wind velocity of dust-moving ranges from 3.5 to 10.9 m/s at the height of 2 m [41]. However, due to the difference in surface dust contents and land use types, dust activity is more frequent in the study site [5]. In this paper, 3.5 m/s is selected as the critical wind speed of dust-moving. During the daytime, the distribution of the wind direction and wind speed at the study site is shown in Figure 3.

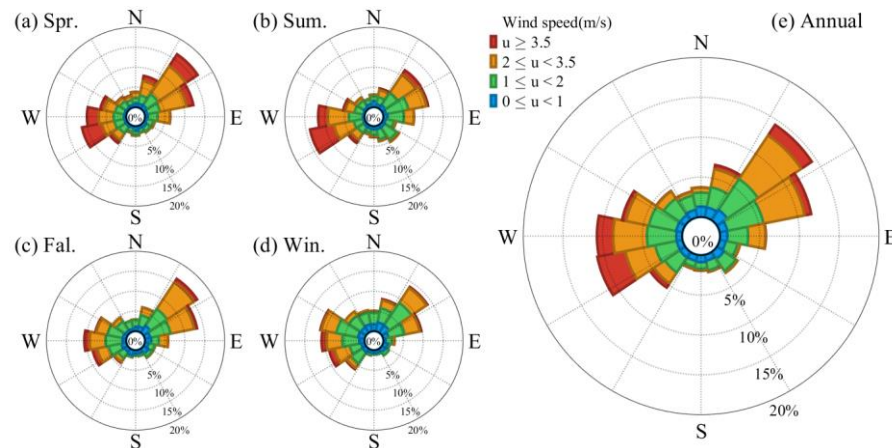


Figure 3. The seasonal and annual wind frequency rose diagrams during the daytime. (a) Spring. (b) Summer. (c) Fall. (d) Winter. (e) Annual.

It can be seen from Figure 3e that the study site is a dual wind type, the east-pathway [42] ($0\text{--}90^\circ$) and west-pathway ($180\text{--}270^\circ$) winds are dominant. The occurrence probability of east-pathway wind (isoline, 15%) is greater than that of west-pathway wind (isoline, 10%). The TD is located in the mid-latitude region of the northern hemisphere, which is mainly controlled by the westerly atmospheric circulation. The airflow entering the TD from the western valley is prone to form a westerly jet due to the mouth effect [43,44]. When the westerly jet encountered the blocking effect of the TP (Figure 1), the westerly wind deflects into the stronger southwest wind (>3.5 m/s) with a high probability of occurrence. Due to the blocking effect of the Tianshan Mountains in the northern TD, a part of the westerly airflow is poured into the eastern part of the desert with a lower altitude and flatter ground, forming the easterly wind [12,45]. The east-west airflow on the surface converges and rises at the study site, resulting in extremely strong wind-sand activity in this area. The probability of the north wind crossing the Tianshan Mountains and the south wind crossing the TP is low. In spring, the frequent occurrence of east-west pathway airflow with high wind speed makes the wind-sand activity more intense [46]. The strong west-pathway wind dominates in summer. Autumn is mainly controlled by the slowing east-pathway airflow. The wind speed is weakest during the daytime in winter.

3.2. Monthly Variation Characteristics

At the study site during the daytime, the average hourly change in MLH and SMEs in different months is shown in Figure 4. The main way of energy exchange of the land-atmosphere is turbulent sensible heat in the TD [10,47]. From the perspective of the time span, between 8:00 and 14:00 BJT, with the increase in temperature and wind speed, the ML rises rapidly (Figure 4a). From 14:00 to 17:00 BJT, the change in amplitude of all SMEs is small (Figure 4b–e), and the MLH is always maintained in a high range. From 17:00 to 20:00 BJT, due to the dust aerosols in the atmosphere increasing the surface energy [48], the atmospheric cooling rate is slow (Figure 4b). However, the decrease in the desert surface temperature is much higher than that of the upper atmosphere, which can promote the formation of the inversion layer, and combined with the sharply decreasing wind speed (Figure 4e), the MLH decreases rapidly.

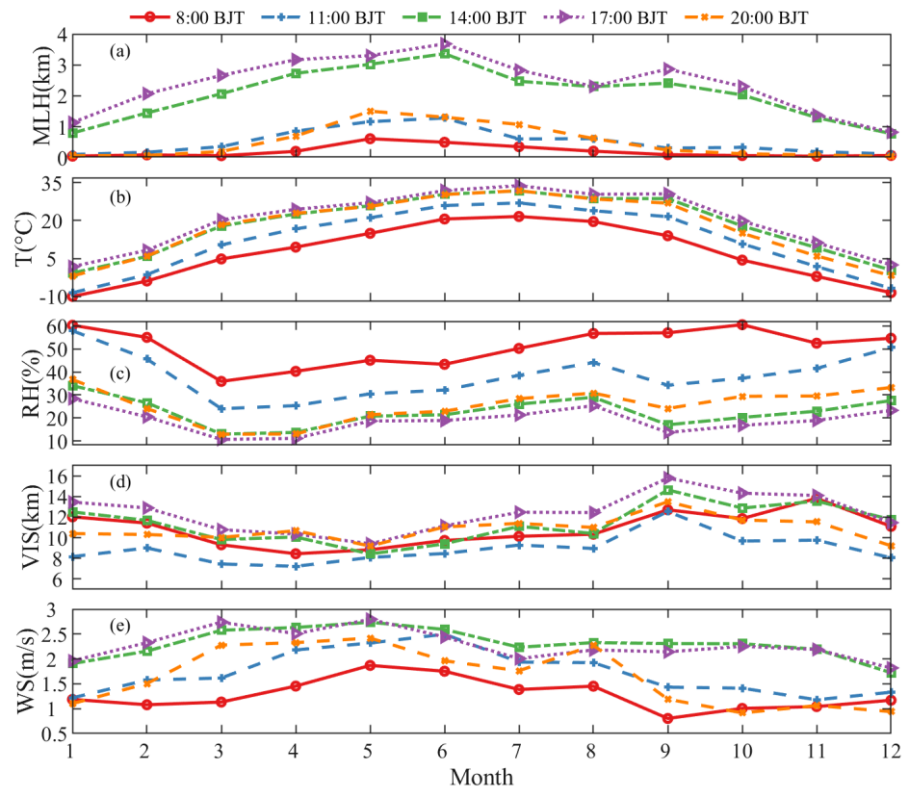


Figure 4. During the daytime, the average hourly change in the mixing layer height and various surface meteorological elements in different months. (a) Mixing layer height. (b) Atmospheric temperature. (c) Relative humidity. (d) Horizontal visibility. (e) Near-surface wind speed. The data at 8:00 BJT represent the monthly average of the whole hour, and the data of other hours are the same.

The monthly average height of the ML reaches its highest at 17:00 BJT. At this moment, the temperature warms up and the wind is strong (2.74 m/s, Figure 4e) in March, which accelerates the evaporation of water and leads to the largest decrease in air relative humidity. In May, the wind speed is the strongest (2.8 m/s, Figure 4e), and the visibility is the lowest among all months (9.4 km, Figure 4d). The warmest month is July (33.83 °C, Figure 4b), but the highest MLH is in June (3.68 km, Figure 4a). From June to July, although the changes in temperature, relative humidity, and visibility are not significant, the wind speed decrease at the highest rate of all months, thus affecting the degree of turbulent mixing in the ML. From August to September, the desert underlying surface absorbed much heat in summer and began to release heat in September, causing the temperature to rise slightly (30.40–30.61 °C, Figure 4b). At the same time, the relative humidity and visibility changed the most among all months (Figure 4c,d), and MLH showed an increasing trend. From September to December, the cooling of the atmosphere and the decrease in solar radiation led to the rapid decrease in temperature (30.61–2.45 °C, Figure 4b).

3.3. Seasonal Variation Characteristics

During the daytime, the average hourly changes in MLH and SMEs across different seasons are shown in Figure 5. It can be seen in Figure 5a that the highest average hourly MLH (2.98 km) appeared at 17:00 BJT in spring and at 16:00 BJT in other seasons. Taking 16:00 BJT as the center point, the MLH presents a unimodal distribution, and the MLH decreases more rapidly in the afternoon than it increases before noon. The MLH is the highest in spring and summer, followed by autumn, and the lowest in winter.

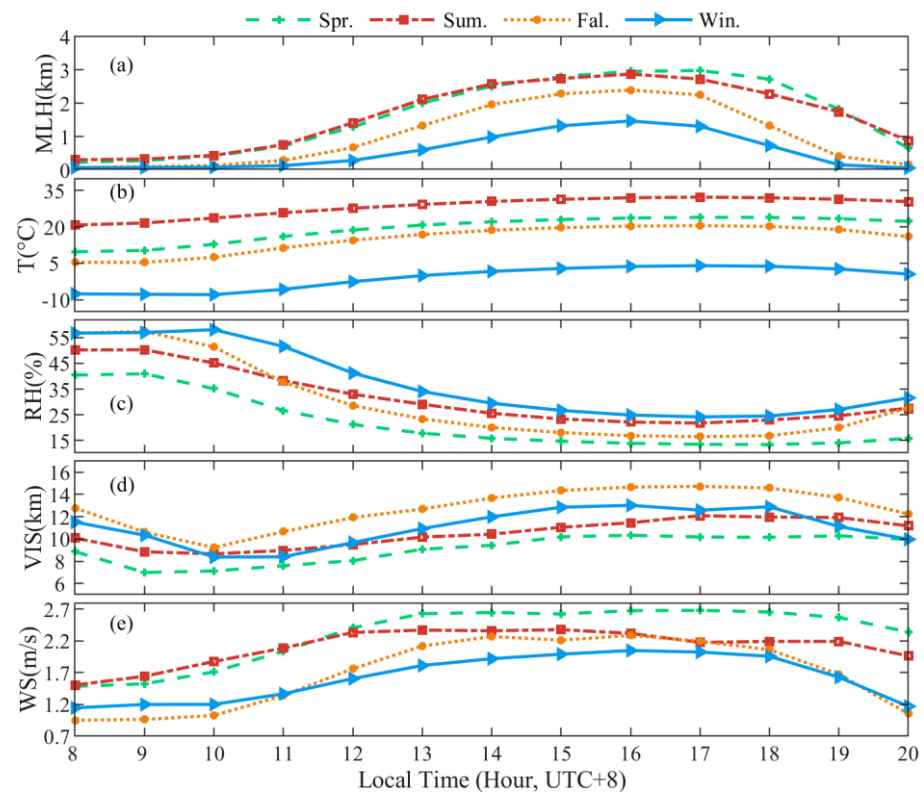


Figure 5. During the daytime, the average hourly change in the mixing layer height and various surface meteorological elements across different seasons. (a) Mixing layer height. (b) Atmospheric temperature. (c) Relative humidity. (d) Horizontal visibility. (e) Near-surface wind speed.

In spring, firstly, the cold air activity is frequent and intense (maximum wind speed 2.68 m/s, 17:00 BJT). Secondly, it can be found in Figure 5b that the temperature rises rapidly from winter to spring after the underlying surface is heated by solar radiation, which can accelerate the freeze–thaw alternation of soil. Finally, the combination of the two roles can accelerate the exchange of land–air material and energy, resulting in rapid development of the ML (Figure 5a). Due to frequent sand–dust weather, visibility is the lowest in spring (Figure 5d). In summer, the precipitation in the study area is the most concentrated, and the surface evaporation is high, so the relative humidity at 15:00–18:00 BJT is similar to that in winter (Figure 5c). The characteristics of dust underlying the surface in summer have the most significant heating effect on the atmosphere (32.31 °C, 17:00 BJT), and the distribution characteristics of MLH in summer are similar to those in spring (Figure 5a). Fall is the transition season, and this season has the best visibility (Figure 5d). As the near-surface layer cools in fall, the atmosphere becomes more stable, and the development of the ML is gradually suppressed. In winter, the rapid cooling and unique basin topography enable the lower desert atmosphere to form an inversion layer [49], and coupled with soil freezing and wind speed slowing, the average MLH is the lowest in each season.

4. Probability Distribution and Relation

The height of the ML is generally below 2–3 km [50]. However, over the TD, a deep ML exceeding 3 km occurred frequently, and the height can even reach 5 km [10,11]. Based on the baseline of 3 km, the MLH is divided into different height intervals for statistical and probabilistic analysis. As shown in Table 2, the corresponding SMEs are divided according to China’s national meteorological standards, such as the ‘Classification of sand and dust weather, GB/T 20480-2017’, ‘Grade of surface air temperature assessment, GB/T 35562-2017’, etc. In this paper, MLH exceeding 4 km are is as deep ML; a temperature greater than 28 °C is classified as hot weather; a relative humidity range of less than 10% corresponds to an extremely dry environment; dust weather mainly consists of floating

dust, followed by blowing dust and dust storms [4], and according to the national standard, visibility below 1 km is usually associated with sandstorms, while visibility between 1 and 10 km is most likely associated with floating dust or blowing dust; and the wind speed of 3.5 m/s is classified as the critical wind speed of dust-moving.

Table 2. The division ranges for MLH and surface meteorological elements.

	MLH (km)	T (°C)	RH (%)	VIS (km)	WS (m/s)	WD (°)
I	[0, 1)	[−25, 0)	[0, 10)	[0, 1)	[0, 1)	[0, 90)
II	[1, 3)	[0, 10)	[10, 20)	[1, 10)	[1, 2)	[90, 180)
III	[3, 4)	[10, 20)	[20, 40)	[10, 20)	[2, 3.5)	[180, 270)
IV	[4, 6]	[20, 28)	[40, 60)	[20, 30]	[3.5, 9]	[270, 360)
V		[28, 45]	[60, 100]			

4.1. Probability Distribution

The probability distribution of MLH and SMEs in each month and season during the daytime is as shown in Figure 6. In spring, from the perspective of temperature and humidity (Figure 6b,c), the temperature increase rate from March to May was the fastest, and the proportion of relative humidity below 10% was the highest (28.41%). In terms of wind speed (Figure 6e), the proportion of wind speed greater than 3.5 m/s reached 17.56% in spring, which was the highest in each season, and May was the month with the strongest wind speed (>3.5 m/s, 21.84%). The proportion of visibility (Figure 6d) less than 10 km and less than 1 km in spring reached 62.12% and 3.35%, respectively, which were the highest percentages in all seasons. The material, thermal, and dynamic conditions in spring were sufficient, and the proportion of MLH higher than 3 km reached 22.13% (Figure 6a), which indicates that the development of ML was the most vigorous in this season.

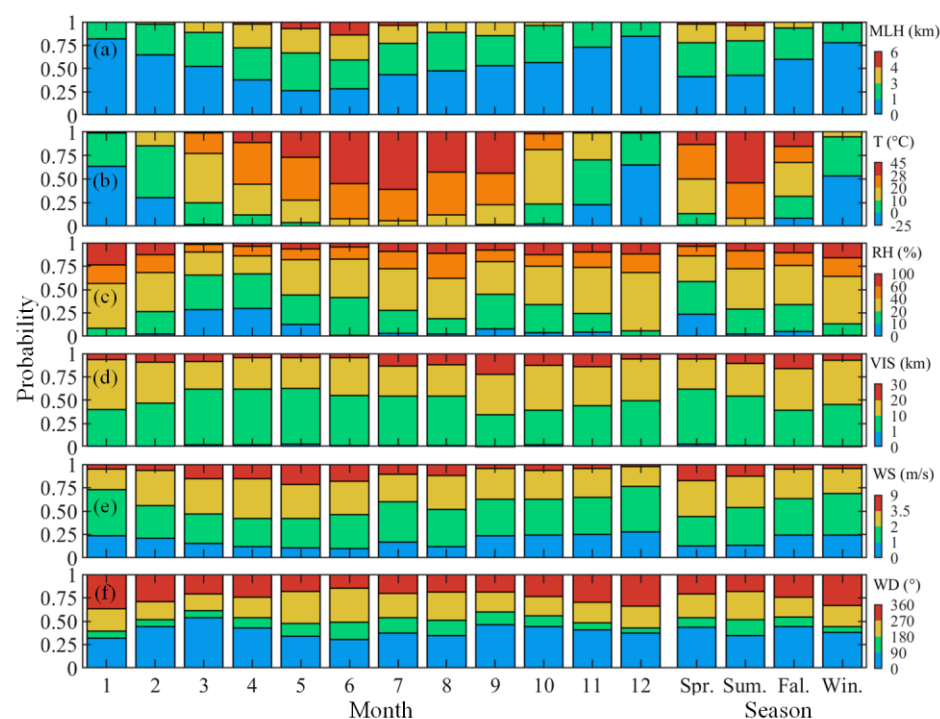


Figure 6. During the daytime, the probability distribution of the mixing layer height and various surface meteorological elements in each month and season. (a) Mixing layer height. (b) Atmospheric temperature. (c) Relative humidity. (d) Horizontal visibility. (e) Near-surface wind speed. (f) Near-surface wind direction.

In summer, most of the time was dominated by hot weather ($>28\text{ }^{\circ}\text{C}$, 53.77%), the proportion of west-pathway wind was the highest in the whole season (30.01%), and the distribution characteristics of MLH were similar to those in spring ($>3\text{ km}$, 20.38%). On the one hand, the long-term high temperature made the temperature of the underlying surface much higher than that of the upper atmosphere, which is easy to form thermal convection; on the other hand, the thermal pump effect of the TP can produce convergent updrafts and lift dust [51–53], thus promoting the development of the ML. The most frequent deep ML formed in June ($>4\text{ km}$, 13.8%) [29].

In fall, the rapid cooling led to a monthly increase in relative humidity, the visibility was the best ($>10\text{ km}$, 61%), the wind speed was small ($<3.5\text{ m/s}$, 94.86%), the atmospheric stability was improved, and the development of the ML was suppressed ($<1\text{ km}$, 60%).

In winter, the temperature was the lowest ($<0\text{ }^{\circ}\text{C}$, 53.68%), the relative humidity was the highest ($>20\%$, 86.79%), the wind speed was the smallest ($<3.5\text{ m/s}$, 95.47%), the soil was easier to freeze, and the MLH was maintained at a lower height ($<1\text{ km}$, 77.62%).

From an annual perspective, both the east-pathway airflow (39.67%) and west-pathway airflow (24.86%) occurred frequently, the proportion of visibility less than 10 km in the study site reached 48.9%, the wind speed was high ($>3.5\text{ m/s}$, 10.04%), and the MLH was relatively low ($<1\text{ km}$, 55.37%). The study site was deeply affected by dust weather.

4.2. Relation Analysis

Figure 7 shows the contribution degree of SMEs to the MLH at different height intervals. From the temperature perspective (Figure 7a), the cold temperature (T1) makes the dust pollutants difficult to spread and contributes the most to the MLH1. The high temperature (T5) provides sufficient thermal conditions for the development of the ML, and the deep ML develops vigorously (MLH4). With the increase in temperature, the contribution degree to MLH1 and MLH4 showed a decreasing and increasing trend, respectively.

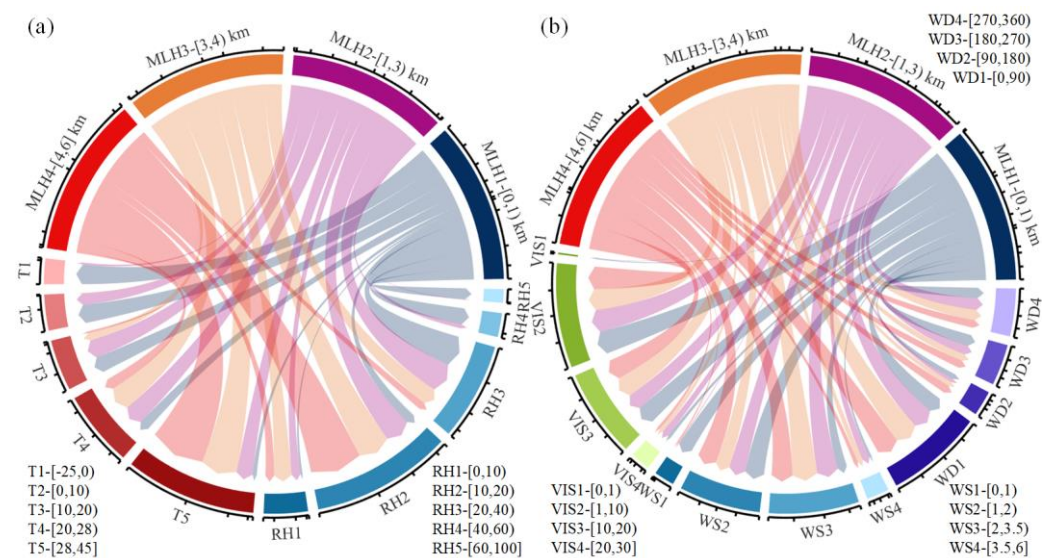


Figure 7. During the daytime, the contribution degree of surface meteorological elements to the mixing layer height at various height intervals. (a) The MLH and its corresponding atmospheric temperature (T) and relative humidity (RH). (b) The MLH and its corresponding horizontal visibility (VIS), near-surface wind speed (WS) and near-surface wind direction (WD). The beginning and end of the arrow indicate two related variables. The width of the arrow trunk signifies the degree of contribution to the mixing layer height, where a wider arrow trunk indicates a greater contribution.

In an extremely dry environment (RH1, Figure 7a), it is conducive to the development of MLH3, but the effect on MLH4 is not obvious. The reason may be that when the atmospheric water vapor content in the desert is very low, the dust aerosol content will dominate, which will lead to the increase of the vertical temperature gradient of the atmosphere and

weaken the atmospheric convective activity. In the relatively dry environment (RH2), it plays a role in promoting the development of the ML higher than 1 km, specifically the MLH4. In a relatively humid environment (RH4 and RH5), the hygroscopic growth of dust particles is easier, the atmospheric stability can be enhanced, and the height distribution of the ML is low (MLH1).

The invasion of cold air often leads to the generation of dust storms (VIS1), and the large amount of dust in the atmosphere can greatly weaken the solar radiation reaching the surface and hinder the penetration of laser beams, resulting in a low MLH distribution (MLH1, Figure 7b). The visibility of floating dust and blowing dust weather falls within the range of VIS2, which has sufficient contribution to all types of MLH. The probability of occurrence of excellent atmospheric visibility (VIS4) in the desert is low, and the effect on the MLH is not significant.

When the horizontal wind speed is small (WS1, Figure 7b), on the one hand, the friction or retardation of the air flow mediated by the underlying surface will be more obvious, thus limiting the vertical mixing air; on the other hand, the weakening of the cooling effect of wind on the ground may reduce the temperature gradient of the atmosphere; finally, the MLH is generally distributed at a lower height (MLH1). With the increase in wind speed, the contribution to MLH1 gradually decreased. WS2 and WS3 belong to the wind speed range defined by floating dust weather, and both have different degrees of effects on the MLH higher than 1 km. It is easier to form dust storm weather when the wind speed falls within the range of WS4.

Compared with the strong west-pathway airflow (WD3, Figure 7b), the east-pathway airflow (WD1) has a greater impact on the deep ML (MLH4). Since WD1 is adapted to the inertial oscillation mechanism of the low-level jet [54], the low-level jet can contain more momentum, strengthen wind shear, and promote the development of the ML in the TD [11,13,55,56]. The gravity effect of the cold air, the different cooling amplitude on the slope terrain, and the foehn effect of the TP will lead to the generation of the downhill airflow (WD2), and the downhill airflow can enhance the turbulence intensity and contribute to MLH4 [29]. The thermal pump effect of the TP [51] and the blocking and lifting of the mountains will form the uphill airflow (WD4), which has an effect on MLH at different heights.

Compared with the cold season (fall and winter), the study site in the warm season (spring and summer) has a higher temperature, higher wind speed, higher MLH, and lower visibility (Figures 5 and 6), thus resulting in more serious dust pollution. Figure 8 shows the probability density distribution between the MLH and the SMEs in the warm season. In the preprocessing stage, the invalid values of SMEs are first removed. Secondly, since the temporal resolution of SMEs is 1 h, the calculated MLH represents the average value within 1 h. Finally, the total number of valid samples during the daytime is 3410.

In the warm season, the temperature distribution in the desert ranges from -5°C to 45°C , which represents a large temperature difference. In particular, the temperature is mainly concentrated in the range of 15°C to 30°C (Figure 8a). When the MLH is lower than 2 km, the relative humidity is concentrated within the range of -10% to 50% . However, when the MLH exceeds 2 km, the center of the relative humidity distribution is located near 15% (Figure 8b). The wind speed is mostly distributed below 2 m/s (Figure 8c), which meets the wind speed requirements for floating dust weather. According to the national meteorological standard, weather with visibility less than 10 km in the desert is categorized as dust weather, and the proportion of visibility below 10 km (Figure 8d) in the local area is very high. It is worth noting that when the height of ML is approximately 3 km, the temperature (30°C), the relative humidity (15%), the wind speed (2 m/s), and the visibility (5 km) all show a clear trend of a concentrated distribution, which indirectly supports the research of Qing He [9] on the existence of a dust layer at the height of 3 km. From the analysis of the MLH, it is evident that during the daytime of the warm season, the MLH is widely distributed between 2 km and 4 km. A higher MLH is conducive to the upward diffusion and dilution of dust particles, thereby increasing the likelihood of dust

transport to greater heights and distances, ultimately affecting the air quality, climate, and environment in the surrounding areas.

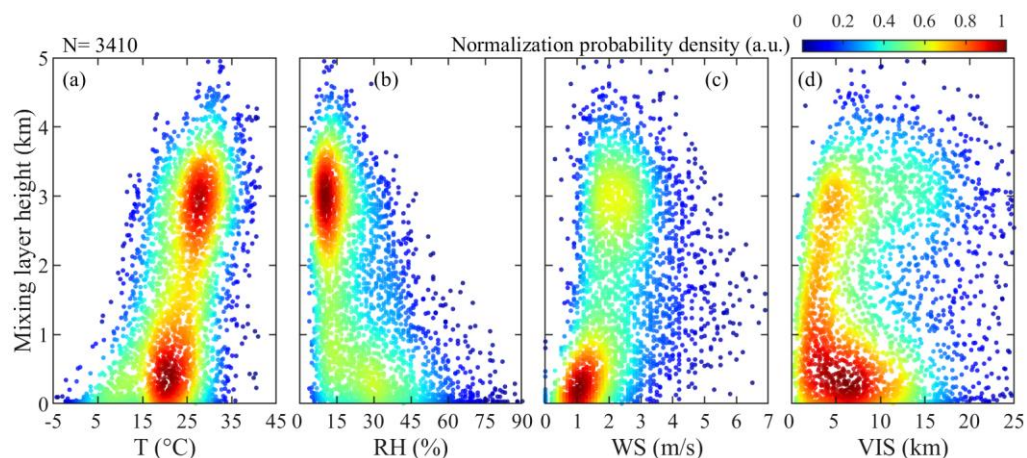


Figure 8. During the daytime, the probability density distribution between the hourly mean mixed layer height and the ground meteorological elements in spring and summer. (a) Atmospheric temperature versus MLH. (b) Relative humidity versus MLH. (c) Near-surface wind speed versus MLH. (d) Horizontal visibility versus MLH.

5. Conclusions

Using CDWL, a two-year stable observation experiment was conducted out on the southern edge of the TD. The MLH during the daytime was retrieved by using the TKEDR threshold method and statistically analyzed with the wind speed, wind direction, atmospheric temperature, relative humidity, and horizontal visibility obtained from the ground weather station. It is found that the proportion of horizontal visibility (<10 km), wind speed (>3.5 m/s), and MLH (<1 km) in the daytime of the study site reached 50.7%, 10.19%, and 56.96%, respectively. These data fully illustrate the severity of local dust pollution.

From the hourly analysis of the daytime, the average maximum MLH occurs between 16:00 BJT and 17:00 BJT. The MLH exhibits a unimodal distribution, and the decrease rate of the MLH after noon is much greater than the increase rate before noon due to the characteristics of the desert underlying surface.

In terms of the average monthly change in data, the average wind speed in March increased most significantly and peaked at 2.8 m/s in May. Although the average temperature reached its highest point in July (33.83 °C), the average wind speed was stronger in June, and the deep ML (>4 km) was also formed most frequently. From September to December, the cooling rate is fast (from 30.61 °C to 2.45 °C).

From the seasonal perspective, the daytime winds at the study site were dominated by west-pathway (the probability of occurrence is 24.86%) and east-pathway (39.67%) winds due to the blocking effect of the Tibetan plateau and the surrounding mountains. Although the average daytime temperature was the highest in summer, the strong east-pathway airflow and west-pathway airflow occurred more frequently in spring, which made the distribution characteristics of MLH in spring (>3 km, 22.13%) similar to those in summer (>3 km, 20.38%).

In the analysis of the relationship between MLH and surface meteorological elements, high temperatures (>28 °C) provide sufficient thermal conditions for the development of the ML. The relative humidity that most contributes to MLH higher than 3 km ranges between 10% and 20%. In conditions of floating dust or blowing dust weather, with visibility ranging from 1–10 km, the ML is significantly influenced. Compared with the stronger west-pathway airflow, the east-pathway airflow conforms to the mechanism of the low-level jet, which contributes more to the formation of a deep ML. When specifically considering MLH around 3 km, there is a clear trend of a concentrated distribution in temperature and relative humidity.

Overall, the study results reveal the distribution characteristics of daytime MLH in the southern edge of the TD and provide important data supplementation for meteorological research on the TD. However, this paper only discussed the influence of near-surface meteorological data on the MLH during the daytime and did not consider the effects of nighttime conditions, different weather patterns, and varying heights on the MLH. The follow-up work will combine the multi-source data to further explore the variation under different weather conditions, as well as the differences between the uphill airflow and the downhill airflow during the ML development.

Author Contributions: Conceptualization, H.X.; methodology, L.S. and J.Y.; experiment, L.S.; software, L.S.; formal analysis, L.S.; investigation, L.S. and Y.W.; resources, L.S., A.M. and Q.H.; data curation, L.S.; writing—original draft preparation, L.S.; writing—review and editing, H.X., J.Y., Y.W., A.M. and Q.H.; visualization, L.S.; supervision, H.X. All authors have read and agreed to the published version of the manuscript.

Funding: This research received no external funding.

Data Availability Statement: The raw data supporting the conclusions of this article will be made available by the authors on request.

Acknowledgments: Thanks for the support of the Xinjiang Uygur Autonomous Region Meteorological Service and the Desert Meteorological Institute of China Meteorological Administration for field experiment and local meteorological data.

Conflicts of Interest: The authors declare no conflicts of interest.

References

1. Stull, R.B. *An Introduction to Boundary Layer Meteorology*; Springer Science & Business Media: Dordrecht, The Netherlands, 1988; Volume 13.
2. Seibert, P.; Beyrich, F.; Gryning, S.-E.; Joffre, S.; Rasmussen, A.; Tercier, P. Review and intercomparison of operational methods for the determination of the mixing height. *Atmos. Environ.* **2000**, *34*, 1001–1027. [[CrossRef](#)]
3. Coen, M.C.; Praz, C.; Haefele, A.; Ruffieux, D.; Kaufmann, P.; Calpini, B. Determination and climatology of the planetary boundary layer height above the Swiss plateau by in situ and remote sensing measurements as well as by the COSMO-2 model. *Atmos. Chem. Phys.* **2014**, *14*, 13205–13221. [[CrossRef](#)]
4. Zhou, Y.; Gao, X.; Lei, J. Characteristics of Dust Weather in the Tarim Basin from 1989 to 2021 and Its Impact on the Atmospheric Environment. *Remote Sens.* **2023**, *15*, 1804. [[CrossRef](#)]
5. Zu, R.; Xue, X.; Qiang, M.; Yang, B.; Qu, J.; Zhang, K. Characteristics of near-surface wind regimes in the Taklimakan Desert, China. *Geomorphology* **2008**, *96*, 39–47. [[CrossRef](#)]
6. Liu, Z.; Dong, Z.; Zhang, Z.; Cui, X.; Xiao, N. Spatial and temporal variation of the near-surface wind regimes in the Taklimakan Desert, Northwest China. *Theor. Appl. Climatol.* **2019**, *138*, 433–447. [[CrossRef](#)]
7. Aili, A.; Xu, H.; Zhao, X. Health effects of dust storms on the south edge of the Taklimakan Desert, China: A survey-based approach. *Int. J. Environ. Res. Public Health* **2022**, *19*, 4022. [[CrossRef](#)]
8. Yang, X.; Shen, S.; Yang, F.; He, Q.; Ali, M.; Huo, W.; Liu, X. Spatial and temporal variations of blowing dust events in the Taklimakan Desert. *Theor. Appl. Climatol.* **2016**, *125*, 669–677. [[CrossRef](#)]
9. He, Q.; Li, J.; Zhao, T.; Zhang, H.; Meng, L. Observing a dust aerosol layer at a height of 3–4 km above the ground on the southern margin of the Tarim Basin. *Atmos. Environ.* **2023**, *318*, 120236. [[CrossRef](#)]
10. Zhang, L.; Zhang, H.; Li, Q.; Wei, W.; Cai, X.; Song, Y.; Mamtimin, A.; Wang, M.; Yang, F.; Wang, Y. Turbulent mechanisms for the deep convective boundary layer in the Taklimakan Desert. *Geophys. Res. Lett.* **2022**, *49*, e2022GL099447. [[CrossRef](#)]
11. Wang, M.; Xu, X.; Xu, H.; Lenschow, D.H.; Zhou, M.; Zhang, J.; Wang, Y. Features of the deep atmospheric boundary layer over the Taklimakan Desert in the summertime and its influence on regional circulation. *J. Geophys. Res. Atmos.* **2019**, *124*, 12755–12772. [[CrossRef](#)]
12. Meng, L.; Yang, X.-h.; Zhao, T.; He, Q.; Lu, H.; Mamtimin, A.; Huo, W.; Yang, F.; Liu, C. Modeling study on three-dimensional distribution of dust aerosols during a dust storm over the Tarim Basin, Northwest China. *Atmos. Res.* **2019**, *218*, 285–295. [[CrossRef](#)]
13. Ge, J.; Huang, J.; Xu, C.; Qi, Y.; Liu, H. Characteristics of Taklimakan dust emission and distribution: A satellite and reanalysis field perspective. *J. Geophys. Res. Atmos.* **2014**, *119*, 11,772–11,783. [[CrossRef](#)]
14. Chongyi, E.; Yong, W.; Taibao, Y.; Jiankang, H.; Hongchang, H.; Fengmei, Y. Different responses of different altitudes surrounding Taklimakan Desert to global climate change. *Environ. Geol.* **2009**, *56*, 1281–1293. [[CrossRef](#)]
15. Huang, J.; Minnis, P.; Yi, Y.; Tang, Q.; Wang, X.; Hu, Y.; Liu, Z.; Ayers, K.; Trepte, C.; Winker, D. Summer dust aerosols detected from CALIPSO over the Tibetan Plateau. *Geophys. Res. Lett.* **2007**, *34*, L18805. [[CrossRef](#)]

16. Yang, F.; He, Q.; Huang, J.; Mamtimin, A.; Yang, X.; Huo, W.; Zhou, C.; Liu, X.; Wei, W.; Cui, C.; et al. Desert Environment and Climate Observation Network over the Taklimakan Desert. *Bull. Am. Meteorol. Soc.* **2020**, *102*, E1172–E1191. [[CrossRef](#)]
17. Song, M.; Wang, Y.; Mamtimin, A.; Gao, J.; Aihaiti, A.; Zhou, C.; Yang, F.; Huo, W.; Wen, C.; Wang, B. Applicability Assessment of Coherent Doppler Wind LiDAR for Monitoring during Dusty Weather at the Northern Edge of the Tibetan Plateau. *Remote Sens.* **2022**, *14*, 5264. [[CrossRef](#)]
18. Wang, M.Z.; Lu, H.; Ming, H.; Zhang, J. Vertical structure of summer clear-sky atmospheric boundary layer over the hinterland and southern margin of Taklamakan Desert. *Meteorol. Appl.* **2016**, *23*, 438–447. [[CrossRef](#)]
19. Yuan, J.; Xia, H.; Wei, T.; Wang, L.; Yue, B.; Wu, Y. Identifying cloud, precipitation, windshear, and turbulence by deep analysis of the power spectrum of coherent Doppler wind lidar. *Opt. Express* **2020**, *28*, 37406–37418. [[CrossRef](#)] [[PubMed](#)]
20. Zhang, Y.; Wu, Y.; Xia, H. Spatial resolution enhancement of coherent Doppler wind lidar using differential correlation pair technique. *Opt. Lett.* **2021**, *46*, 5550–5553. [[CrossRef](#)]
21. Yuan, J.; Su, L.; Xia, H.; Li, Y.; Zhang, M.; Zhen, G.; Li, J. Microburst, windshear, gust front, and vortex detection in mega airport using a single coherent Doppler wind lidar. *Remote Sens.* **2022**, *14*, 1626. [[CrossRef](#)]
22. Xia, H.; Chen, Y.; Yuan, J.; Su, L.; Yuan, Z.; Huang, S.; Zhao, D. Windshear Detection in Rain Using a 30 km Radius Coherent Doppler Wind Lidar at Mega Airport in Plateau. *Remote Sens.* **2024**, *16*, 924. [[CrossRef](#)]
23. Wang, Z.; Cao, X.; Zhang, L.; Notholt, J.; Zhou, B.; Liu, R.; Zhang, B. Lidar measurement of planetary boundary layer height and comparison with microwave profiling radiometer observation. *Atmos. Meas. Tech.* **2012**, *5*, 1965–1972. [[CrossRef](#)]
24. Kotthaus, S.; Haeffelin, M.; Drouin, M.-A.; Dupont, J.-C.; Grimmond, S.; Haeffele, A.; Hervo, M.; Poltera, Y.; Wiegner, M. Tailored Algorithms for the Detection of the Atmospheric Boundary Layer Height from Common Automatic Lidars and Ceilometers (ALC). *Remote Sens.* **2020**, *12*, 3259. [[CrossRef](#)]
25. Li, H.; Yang, Y.; Hu, X.M.; Huang, Z.; Wang, G.; Zhang, B.; Zhang, T. Evaluation of retrieval methods of daytime convective boundary layer height based on lidar data. *J. Geophys. Res. Atmos.* **2017**, *122*, 4578–4593. [[CrossRef](#)]
26. Wu, Y.-P.; Feng, G.-L.; Li, B.-L. Interactions of multiple atmospheric circulation drive the drought in Tarim River Basin. *Sci. Rep.* **2016**, *6*, 26470. [[CrossRef](#)] [[PubMed](#)]
27. Yang, T.; Wang, X.; Zhao, C.; Chen, X.; Yu, Z.; Shao, Q.; Xu, C.Y.; Xia, J.; Wang, W. Changes of climate extremes in a typical arid zone: Observations and multimodel ensemble projections. *J. Geophys. Res. Atmos.* **2011**, *116*, D19106. [[CrossRef](#)]
28. Sun, J.; Liu, T.-s. The Age of the Taklimakan Desert. *Science* **2006**, *312*, 1621. [[CrossRef](#)]
29. Su, L.; Lu, C.; Yuan, J.; Wang, X.; He, Q.; Xia, H. Measurement report: The promotion of low-level jet and thermal-effect on development of deep convective boundary layer at the southern edge of the Taklimakan Desert. *EGU Sphere* **2024**, *2024*, 1–24. [[CrossRef](#)]
30. Li, M.; Xia, H.; Su, L.; Han, H.; Wang, X.; Yuan, J. The Detection of Desert Aerosol Incorporating Coherent Doppler Wind Lidar and Rayleigh–Mie–Raman Lidar. *Remote Sens.* **2023**, *15*, 5453. [[CrossRef](#)]
31. Wei, T.; Xia, H.; Wu, Y.; Yuan, J.; Wang, C.; Dou, X. Inversion probability enhancement of all-fiber CDWL by noise modeling and robust fitting. *Opt. Express* **2020**, *28*, 29662–29675. [[CrossRef](#)]
32. Banakh, V.; Smalikho, I.; Falits, A. Estimation of the turbulence energy dissipation rate in the atmospheric boundary layer from measurements of the radial wind velocity by micropulse coherent Doppler lidar. *Opt. Express* **2017**, *25*, 22679–22692. [[CrossRef](#)]
33. Banakh, V.A.; Smalikho, I.N. Lidar studies of wind turbulence in the stable atmospheric boundary layer. *Remote Sens.* **2018**, *10*, 1219. [[CrossRef](#)]
34. Smalikho, I.N.; Banakh, V.A. Measurements of wind turbulence parameters by a conically scanning coherent Doppler lidar in the atmospheric boundary layer. *Atmos. Meas. Tech.* **2017**, *10*, 4191–4208. [[CrossRef](#)]
35. Wang, L.; Qiang, W.; Xia, H.; Wei, T.; Yuan, J.; Jiang, P. Robust Solution for Boundary Layer Height Detections with Coherent Doppler Wind Lidar. *Adv. Atmos. Sci.* **2021**, *38*, 1920–1928. [[CrossRef](#)]
36. Vakkari, V.; O'Connor, E.J.; Nisantzi, A.; Mamouri, R.E.; Hadjimitsis, D.G. Low-level mixing height detection in coastal locations with a scanning Doppler lidar. *Atmos. Meas. Tech.* **2015**, *8*, 1875–1885. [[CrossRef](#)]
37. Banakh, V.A.; Smalikho, I.N.; Falits, A.V. Estimation of the height of the turbulent mixing layer from data of Doppler lidar measurements using conical scanning by a probe beam. *Atmos. Meas. Tech.* **2021**, *14*, 1511–1524. [[CrossRef](#)]
38. Wang, L.; Yuan, J.; Xia, H.; Zhao, L.; Wu, Y. Marine mixed layer height detection using ship-borne coherent Doppler wind lidar based on constant turbulence threshold. *Remote Sens.* **2022**, *14*, 745. [[CrossRef](#)]
39. Wu, K.; Wei, T.; Yuan, J.; Xia, H.; Huang, X.; Lu, G.; Zhang, Y.; Liu, F.; Zhu, B.; Ding, W. Thundercloud structures detected and analyzed based on coherent Doppler wind lidar. *Atmos. Meas. Tech. Discuss.* **2023**, *2023*, 5811–5825. [[CrossRef](#)]
40. Yin, J.; Gu, H.; Huang, J.; Wang, M. An investigation into the vertical structures of low-altitude atmosphere over the Central Taklimakan Desert in summer. *Atmos. Sci. Lett.* **2021**, *22*, e1042. [[CrossRef](#)]
41. Yang, X.; He, Q.; Matimin, A.; Yang, F.; Huo, W.; Liu, X.; Zhao, T.; Shen, S. Threshold velocity for saltation activity in the Taklimakan Desert. *Pure Appl. Geophys.* **2017**, *174*, 4459–4470. [[CrossRef](#)]
42. Chen, Y.; An, J.; Qu, Y.; Xie, F.; Ma, S. Dust radiation effect on the weather and dust transport over the Taklimakan Desert, China. *Atmos. Res.* **2023**, *284*, 106600. [[CrossRef](#)]
43. Zeng, Y.; Yang, L.; Tong, Z.; Jiang, Y.; Chen, P.; Zhou, Y. Characteristics and Applications of Summer Season Raindrop Size Distributions Based on a PARSIVEL2 Disdrometer in the Western Tianshan Mountains (China). *Remote Sens.* **2022**, *14*, 3988. [[CrossRef](#)]

44. Zeng, Y.; Yang, L. Triggering mechanism of an extreme rainstorm process near the Tianshan Mountains in Xinjiang, an arid region in China, based on a numerical simulation. *Adv. Meteorol.* **2020**, *2020*, 8828060. [[CrossRef](#)]
45. Meng, L.; Zhao, T.; He, Q.; Yang, X.; Mamtimin, A.; Wang, M.; Pan, H.; Huo, W.; Yang, F.; Zhou, C. Dust radiative effect characteristics during a typical springtime dust storm with persistent floating dust in the Tarim Basin, Northwest China. *Remote Sens.* **2022**, *14*, 1167. [[CrossRef](#)]
46. Sun, J.; Zhang, M.-Z.; Liu, T.-s. Spatial and temporal characteristics of dust storms in China and its surrounding regions, 1960–1999: Relations to source area and climate. *J. Geophys. Res.* **2001**, *106*, 10325–10333. [[CrossRef](#)]
47. Tan, Z.; Liu, Y.; Zhu, Q.; Bi, J. Effect of dust aerosols on the heat exchange over the Taklimakan Desert. *Atmos. Environ.* **2022**, *276*, 119058. [[CrossRef](#)]
48. Su, S.; Wang, J.; Yin, Z.; Wang, T.; Yasheng, D.; Xie, X.; Sun, C.; Yang, Y. Understanding the Daytime and Nighttime Impacts of Dust Aerosols on Surface Energy and Meteorological Fields in Northwest China. *J. Geophys. Res. Atmos.* **2022**, *127*, e2022JD037619. [[CrossRef](#)]
49. Xu, X.; Wu, H.; Yang, X.; Xie, L. Distribution and transport characteristics of dust aerosol over Tibetan Plateau and Taklimakan Desert in China using MERRA-2 and CALIPSO data. *Atmos. Environ.* **2020**, *237*, 117670. [[CrossRef](#)]
50. Garratt, J.R. The atmospheric boundary layer. *Earth-Sci. Rev.* **1994**, *37*, 89–134. [[CrossRef](#)]
51. Wu, G.; Liu, Y.; Zhang, Q.; Duan, A.; Wang, T.; Wan, R.; Liu, X.; Li, W.; Wang, Z.; Liang, X. The Influence of Mechanical and Thermal Forcing by the Tibetan Plateau on Asian Climate. *J. Hydrometeorol.* **2007**, *8*, 770–789. [[CrossRef](#)]
52. Wu, G.; Liu, Y.; He, B.; Bao, Q.; Duan, A.; Jin, F.F. Thermal Controls on the Asian Summer Monsoon. *Sci. Rep.* **2012**, *2*, 404. [[CrossRef](#)] [[PubMed](#)]
53. Meng, L.; Yang, X.; Zhao, T.; He, Q.; Mamtimin, A.; Wang, M.; Huo, W.; Yang, F.; Zhou, C.; Pan, H. Simulated regional transport structures and budgets of dust aerosols during a typical springtime dust storm in the Tarim Basin, Northwest China. *Atmos. Res.* **2020**, *238*, 104892. [[CrossRef](#)]
54. Blackadar, A.K. Boundary Layer Wind Maxima and Their Significance for the Growth of Nocturnal Inversions. *Bull. Am. Meteorol. Soc.* **1957**, *38*, 283–290. [[CrossRef](#)]
55. Ge, J.M.; Liu, H.; Huang, J.; Fu, Q. Taklimakan Desert nocturnal low-level jet: Climatology and dust activity. *Atmos. Chem. Phys.* **2016**, *16*, 7773–7783. [[CrossRef](#)]
56. Yang, G.; Shu, W.; Wang, M.; Mao, D.; Pan, H.; Zhang, J. Analysis of Height of the Stable Boundary Layer in Summer and Its Influencing Factors in the Taklamakan Desert Hinterland. *Remote Sens.* **2024**, *16*, 1417. [[CrossRef](#)]

Disclaimer/Publisher’s Note: The statements, opinions and data contained in all publications are solely those of the individual author(s) and contributor(s) and not of MDPI and/or the editor(s). MDPI and/or the editor(s) disclaim responsibility for any injury to people or property resulting from any ideas, methods, instructions or products referred to in the content.